Tailoring Ferroelectric Polarization in $In_2Se_nS_{3-n}$ Monolayers via Se/S Ratio Modulation to Boost Polysulfide Electrocatalysis

Haoyun Dou [a], Xuanpan Xu [a], Rawaid Ali [a], Hongqing Ma [b,*], Chen Qing [a,*], Hong-En Wang [a,*]

[a] College of Physics and Electronic Information, Yunnan Key Laboratory of Optoelectronic Information Technology, Yunnan Normal University, 650500 Kunming, China. E-mail: chenqing@ynnu.edu.cn; hongen.wang@ynnu.edu.cn; hongen.wang@outlook.com

[b] School of Energy & Environmental Science, Yunnan Normal University, Kunming 650500, China. E-mail: hongqing6010@126.com

Computational Details

All DFT calculations were carried out using the Vienna ab initio Simulation Package (VASP) code.[1 2] The project augmented wave pseudopotential was adopted to describe the electron−core interaction.[3 4] The exchange-correlation functional of generalized gradient approximation in the form of Perdew-Burke-Ernzerhof (GGA-PBE)[5] was used with a cutoff energy of 400 eV. A 4 × 4 × 1 supercell was built to mitigate the influence of periodic boundary conditions on intermolecular interactions. A 20 Å vacuum layer was established to prevent interference between the upper and lower layers. The *k*-points of 3 × 3 × 1 were used for Brillouin zone integration, employing the Monkhorst-Pack scheme. An empirical DFT-D3 dispersion correction

was employed to include long-range van der Waals (vdW) interactions.[6] All structural geometries were optimized until the maximal residual energy and force were less than 1×10^{-5} eV and 0.01 eV/Å, respectively.

Polarization is described by modern polarization theory. It is common to divide the total polarization of the material into the ionic (P_i) and electronic (P_e) parts:

$$P_i = \frac{|e|}{\Omega}\sum_v Z_{ion}^{v} r^{v} \#(1)$$

where Z_{ion}^{v} and r^{v} are the valence charge and position vector of atom v, Ω is the unit cell volume, and the sum runs over all ions in the unit cell.

$$P_e = \frac{2|e|i}{(2\pi)^3}\oiint dk_{\perp}\sum_{n=1}^{M}\int_0^{G_{\parallel}}\left\langle \mu_{k,n}\left|\frac{\partial}{\partial k_{\parallel}}\right|\mu_{k,n}\right\rangle dk_{\parallel} \#(2)$$

where the sum runs over the occupied bands, $k_{\perp}$ is perpendicular to the polarization direction, $k_{\parallel}$ is parallel to the direction of the polarization, and $G_{||}$ is a reciprocal lattice vector in the same direction. The states $|\mu_{k,n}\rangle$ are the cell-periodic parts of the Bloch functions.

The total polarization (P_t) is simply the sum of P_i and P_e:

$$P_t = P_i + P_e \#(3)$$

For the $In_2Se_nS_{3-n}$ material, the ferroelectric phase is the α-phase, whereas the centrosymmetric phase is the β-phase, with the polarization intensity of the material obtained via the Berry phase method.

The binding strength between $In_2Se_nS_{3-n}$ and LiPSs is determined by the following equation:

$$E_b = E_{total} - (E_{In_2Se_nS_{(3-n)}} + E_{polysulfides}) \#(4)$$

Where E_{total}, $E_{\text{polysulfides}}$, and $E_{In_2Se_nS_{(3-n)}}$ denote the energies of polysulfide-adsorbed $In_2Se_nS_{(3-n)}$, LPSs, and $In_2Se_nS_{(3-n)}$, respectively. The contributions of van der Waals (vdW) and chemical (chem) interactions to the total adsorption energy were calculated by including vdW corrections in VASP. The total adsorption energy was computed with vdW corrections, after which the chemical interaction energy was

determined without vdW corrections. The vdW energy was then obtained by subtracting the chemical interaction energy from the total adsorption energy.[7]

The overall equation for the conversion of S_8 to Li_2S is:

$$S_8 + 16Li^+ + 16e^- \rightleftharpoons 8Li_2S \#(5)$$

The discharging process comprises six elementary steps from S_8 to Li_2S.

$$S_8 + 2Li^+ + 2e^- \rightarrow Li_2S_8 \#(6)$$

$$3Li_2S_8 + 2Li^+ + 2e^- \rightarrow 4Li_2S_6 \#(7)$$

$$2Li_2S_6 + 2Li^+ + 2e^- \rightarrow 3Li_2S_4 \#(8)$$

$$Li_2S_4 + 2Li^+ + 2e^- \rightarrow 2Li_2S_2 \#(9)$$

$$Li_2S_4 + 6Li^+ + 6e^- \rightarrow 4Li_2S \#(10)$$

$$Li_2S_2 + 2Li^+ + 2e^- \rightarrow 2Li_2S \#(11)$$

The reaction Gibbs free energy of each step is evaluated according to:[8]

$$\triangle G = \triangle E + \triangle E_{ZPE} - T \triangle S \#(12)$$

where $\triangle E$, $\triangle E_{ZPE}$, and $\triangle S$ represent the difference in adsorption energy, zero-point energy, and entropy, respectively, between the higher-order LiPSs and the lower-order LiPSs. The zero-point energy and entropy are estimated by calculating the vibrational frequency of adsorbed LiPSs. The temperature is set to 300 K. For instance, for the lithiation Li process $*Li_2S_8 \rightarrow *Li_2S_6 + 1/4S_8$, the reaction Gibbs free energy is obtained by the following:

$$\triangle G = \left(E_{*Li_2S_6} + E_{(*Li_2S_6)ZPE} - TS_{*Li_2S_6}\right) + \frac{1}{4\left(E_{*S_8} + E_{(*S_8)ZPE} - TS_{*S_8}\right)} - \left(E_{*Li_2S_8} + E_{(*Li_2S_8)ZPE} - TS_{*Li_2S_8}\right) \#(13)$$

The charging process occurs through the decomposition of Li_2S molecules into Li^+ and LiS^- clusters, as expressed by the reaction $Li_2S \rightarrow Li^+ + LiS^-$.

The mobility of the 2D systems is expressed by:

$$\mu = \frac{e\hbar^3 C}{(m^*)^2 k_B T E_1^2} \#(14)$$

where $\hbar$ is the reduced Planck constant, e is the element charge, C is the elastic matrix constant, m^* is the effective mass of charge, k_B is the Boltzmann constant, T is the temperature, and E_1 is the deformation potential. T is set to be room temperature (T = 300 K). Parameters m^*, E_1, and C for $In_2Se_nS_{(3-n)}$ can be acquired by first-principles computations.

Table S1. Calculated total energies of the six structural isomers of $In_2Se_nS_{3-n}$ (n=1, 2). These isomers were generated by considering all possible single (n=1) and double (n=2) S-for-Se substitutions, enumerating all distinct substitution sites within the In-Se framework. The specific configurations are In_2Se_2S, In_2SeSSe, In_2SSe_2, In_2S_2Se, In_2SSeS, and In_2SeS_2. More negative values indicate greater thermodynamic stability of the corresponding structure.

	In_2Se_2S	In_2SeSSe	In_2SSe_2
Energy (eV)	-19.5359	-19.6259	-19.5402
	In_2S_2Se	In_2SSeS	In_2SeS_2
Energy (eV)	-20.2172	-20.1484	-20.2232

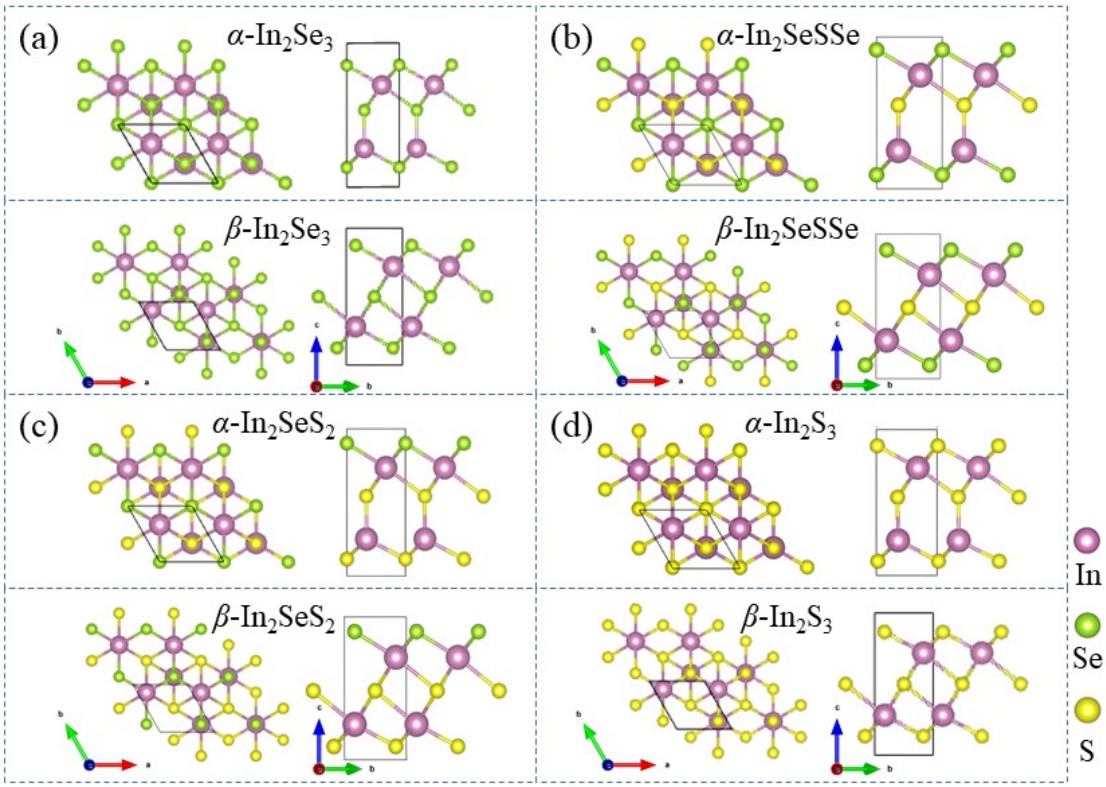

Figure S1. Comparative structural diagrams of the ferroelectric α-phase and paraelectric/reference β-phase. Atomic configurations for (a) In_2Se_3, (b) In_2SeSSe, (c) In_2SeS_2, and (d) In_2S_3.

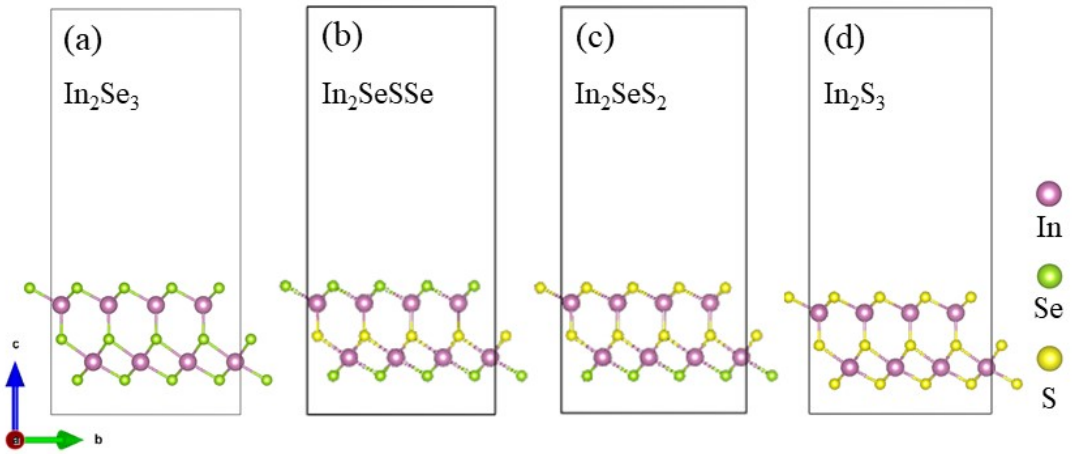

Figure S2. Structural diagram after ferroelectric phase reversal. Atomic configurations for (a) In_2Se_3, (b) In_2SeSSe, (c) In_2SeS_2, and (d) In_2S_3.

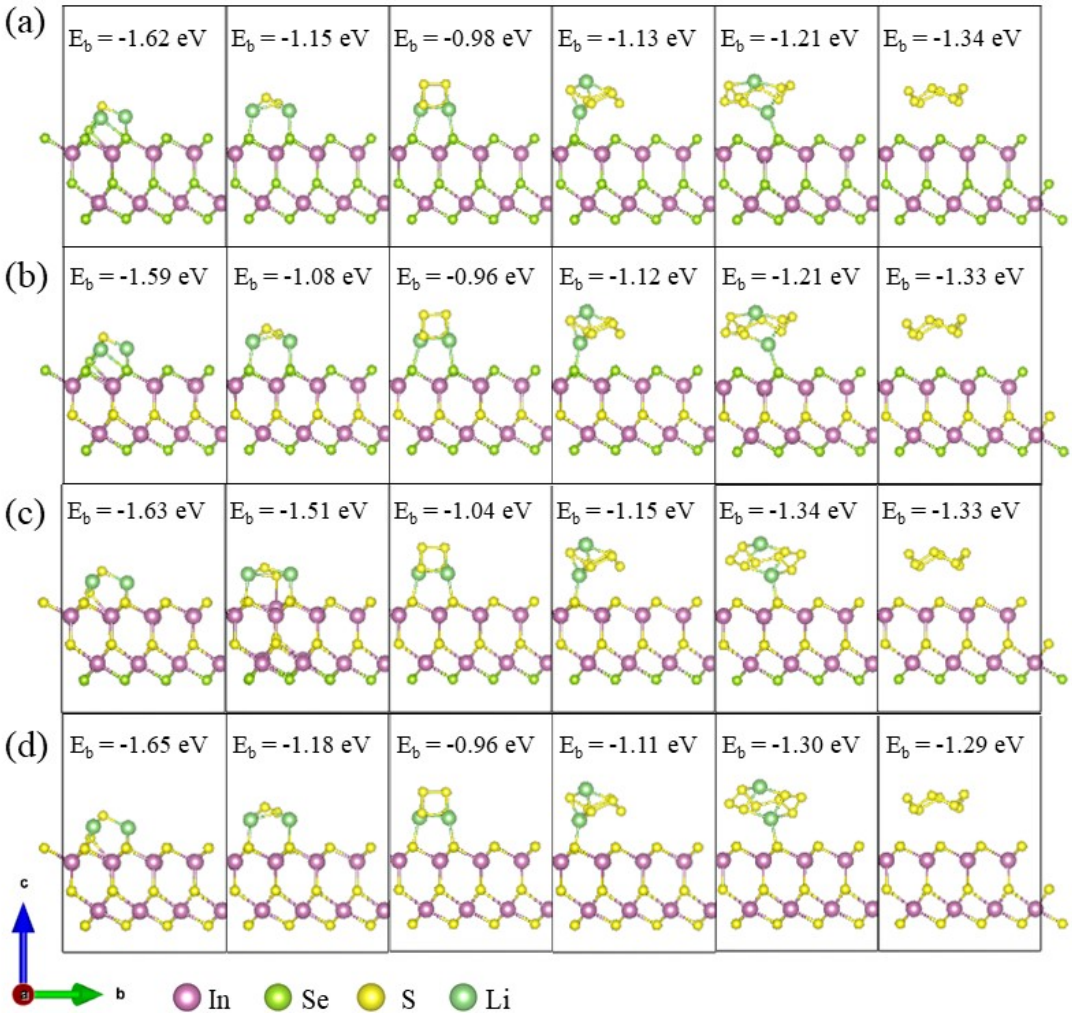

Figure S3. Atomic structural model of a two-dimensional $In_2Se_nS_{3-n}$ catalyst adsorbing lithium polysulfide after ferroelectric reversal. Optimized configurations for (a) In_2Se_3, (b) In_2SeSSe, (c) In_2SeS_2, and (d) In_2S_3.

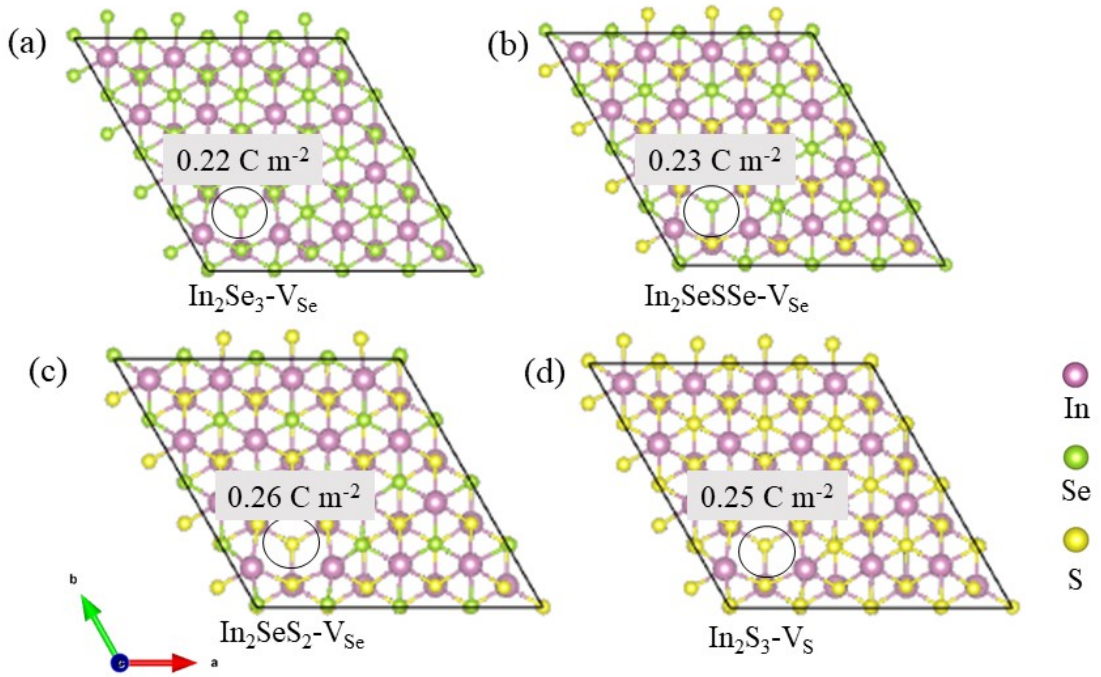

Figure S4. Structural diagram of a ferroelectric phase with Se or S defects on the surface. Atomic configurations for (a) In_2Se_3, (b) In_2SeSSe, (c) In_2SeS_2, and (d) In_2S_3.

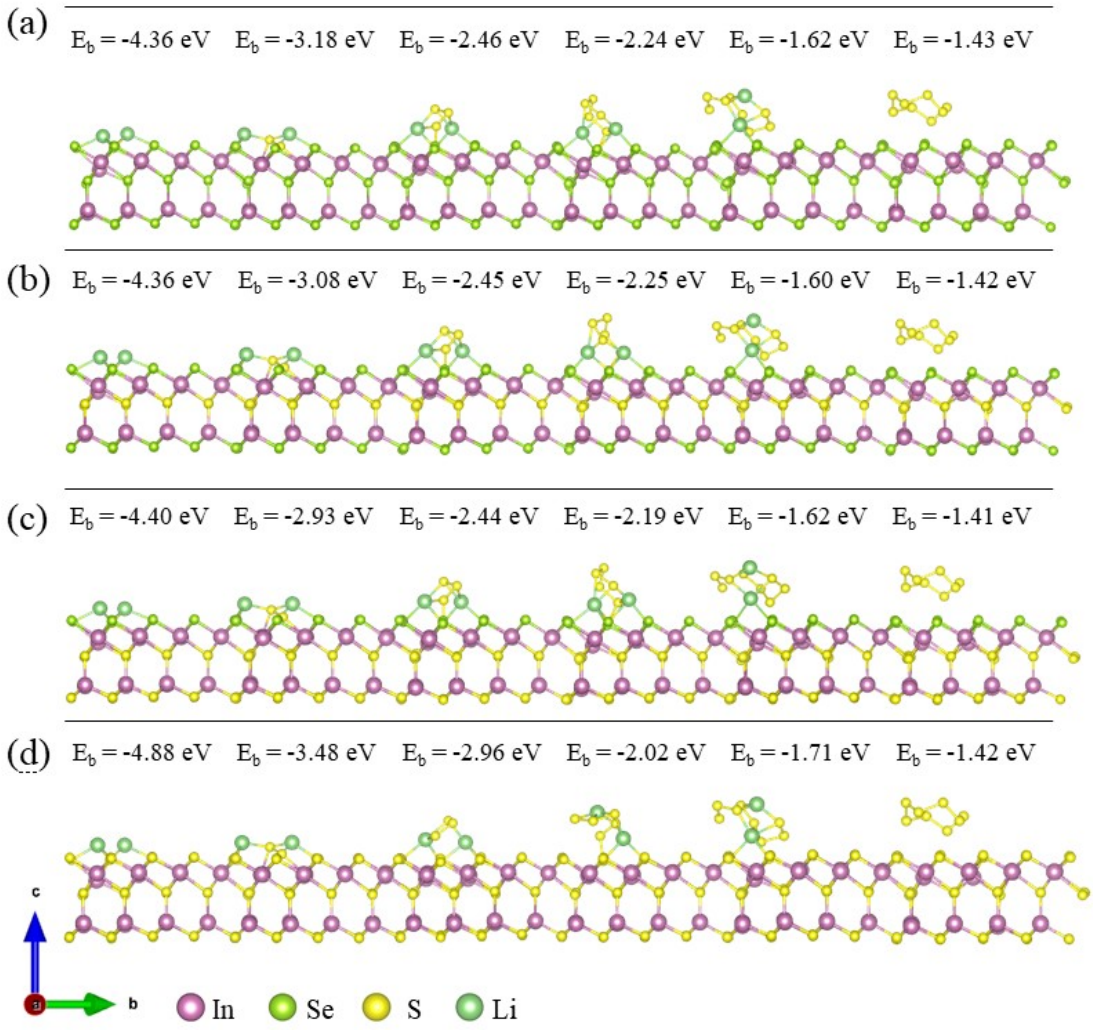

Figure S5. Atomic structural model of lithium polysulfide adsorption on a two-dimensional $In_2Se_nS_{3-n}$ catalyst with surface defects. Optimized configurations for (a) In_2Se_3, (b) In_2SeSSe, (c) In_2SeS_2, and (d) In_2S_3.

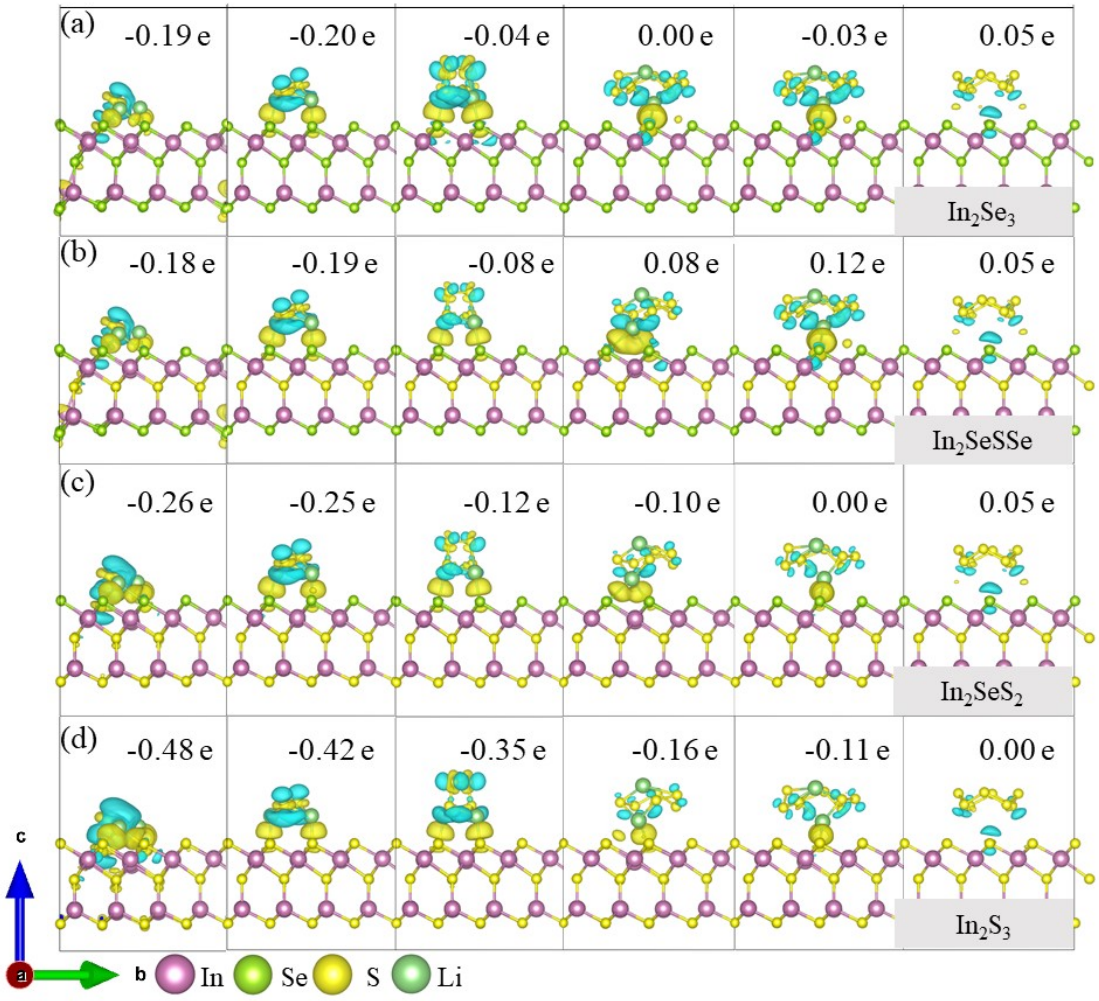

Figure S6. Differential charge density analysis for the adsorption of various sulfur species on $In_2Se_nS_{3-n}$ monolayers. Side views of the optimized atomic configurations and the corresponding differential charge density (Δρ) isosurfaces for (a) In_2Se_3, (b) In_2SeSSe, (c) In_2SeS_2, and (d) In_2S_3 upon adsorbing Li_2S, Li_2S_2, Li_2S_4, Li_2S_6, Li_2S_8, and S_8. The Δρ isosurface level is set at ±0.002 e $Å^{-3}$. Yellow and cyan regions represent electron accumulation and depletion, respectively.

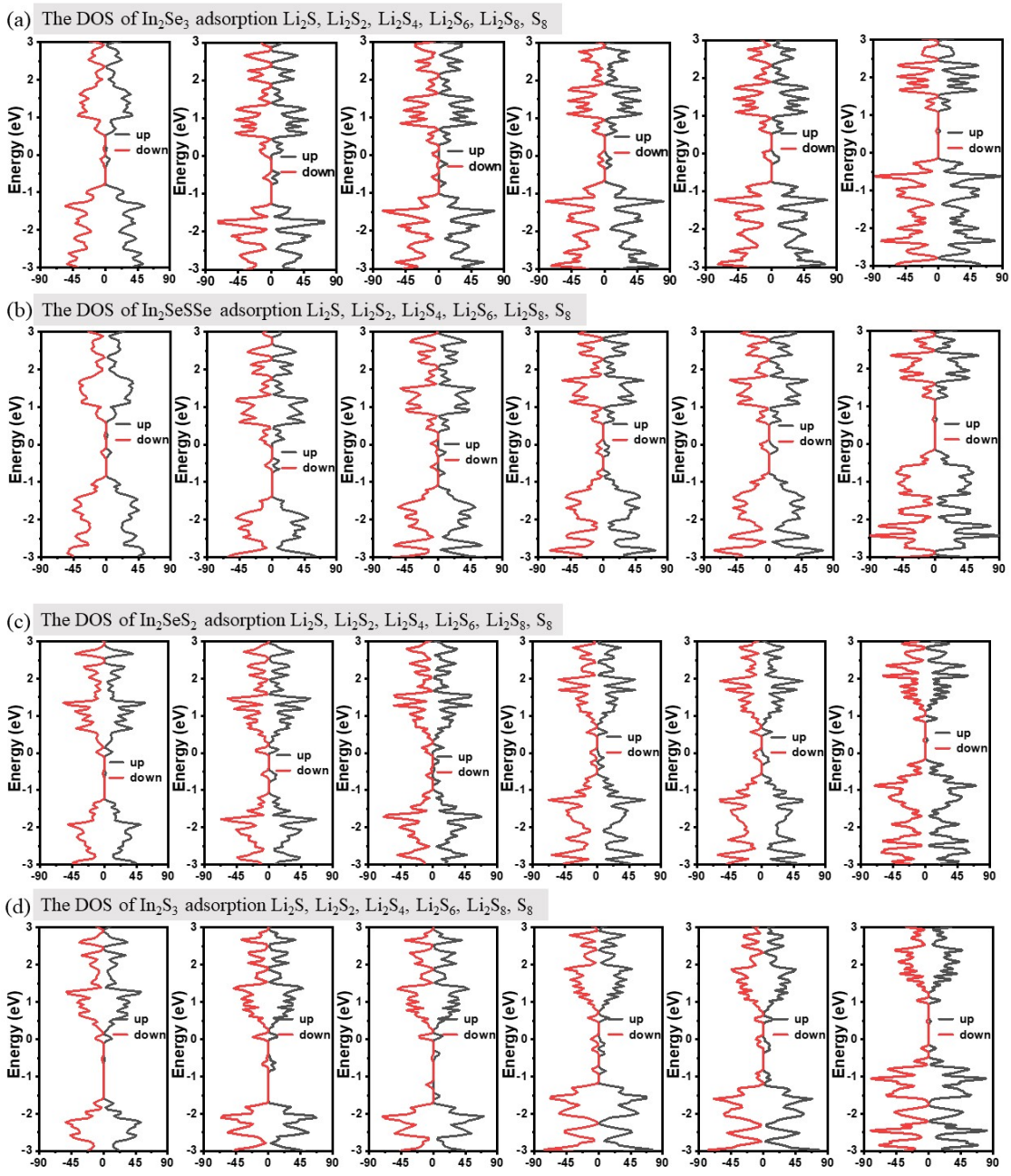

Figure S7. Electronic density of states (DOS) evolution upon polysulfide adsorption. Total DOS for (a) In_2Se_3, (b) In_2SeSSe, (c) In_2SeS_2, and (d) In_2S_3 monolayers before and after adsorbing a series of sulfur species: Li_2S, Li_2S_2, Li_2S_4, Li_2S_6, Li_2S_8, and S_8. In each panel, the red and black curves represent the spin-up and spin-down channels, respectively. The Fermi level is set to 0 eV.

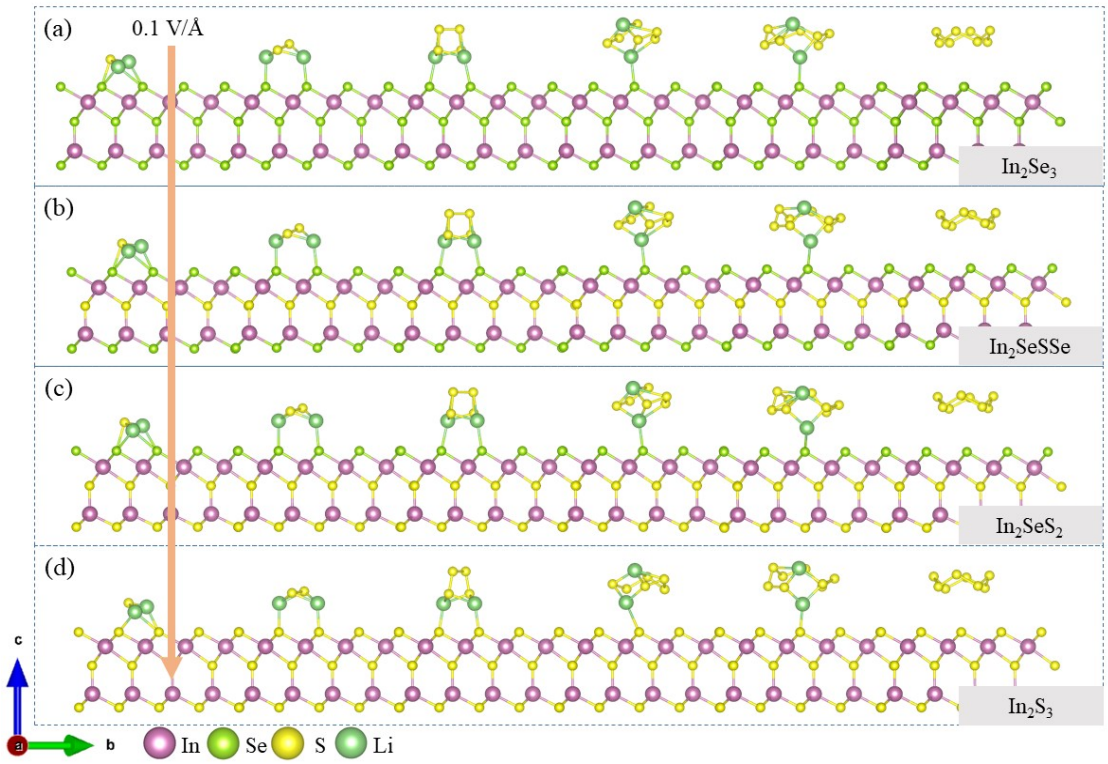

Figure S8. Optimized atomic configurations for polysulfide adsorption on $In_2Se_nS_{3-n}$ monolayers under an external electric field. Side views of the equilibrium structures for (a) In_2Se_3, (b) In_2SeSSe, (c) In_2SeS_2, and (d) In_2S_3 monolayers adsorbing a lithium polysulfide chain, as obtained from DFT calculations with an applied electric field of 0.1 eV $Å^{-1}$. The field direction is indicated by the vertical orange arrow labeled "0.1 V/Å".

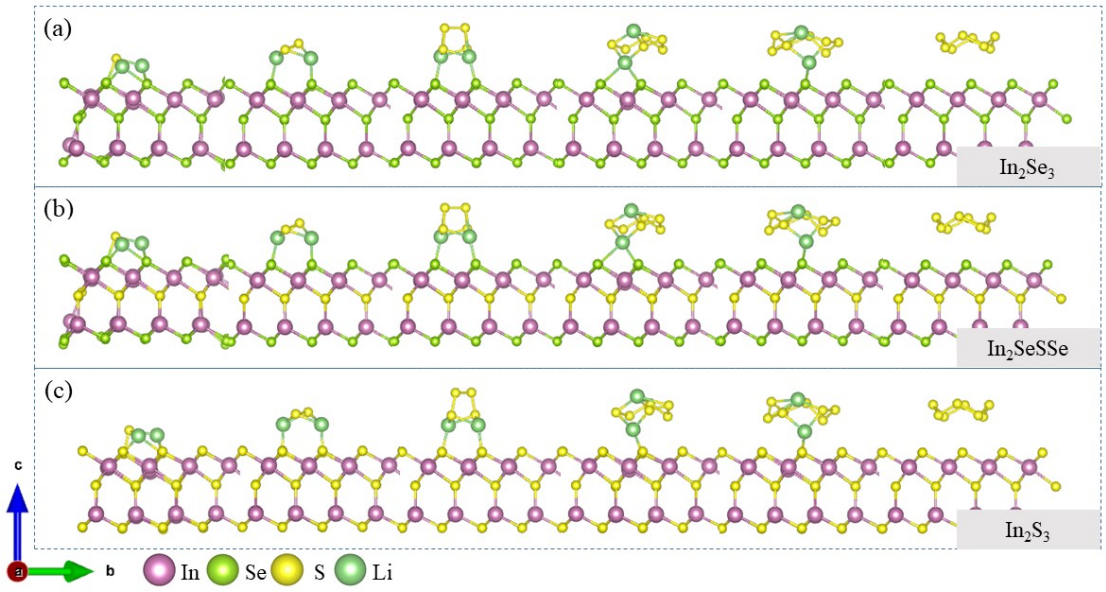

Figure S9. Atomic structure models of lithium polysulfide adsorption on two-dimensional $In_2Se_nS_{3-n}$ catalysts. Optimized configurations for (a) In_2Se_3, (b) In_2SeSSe, and (c) In_2S_3.

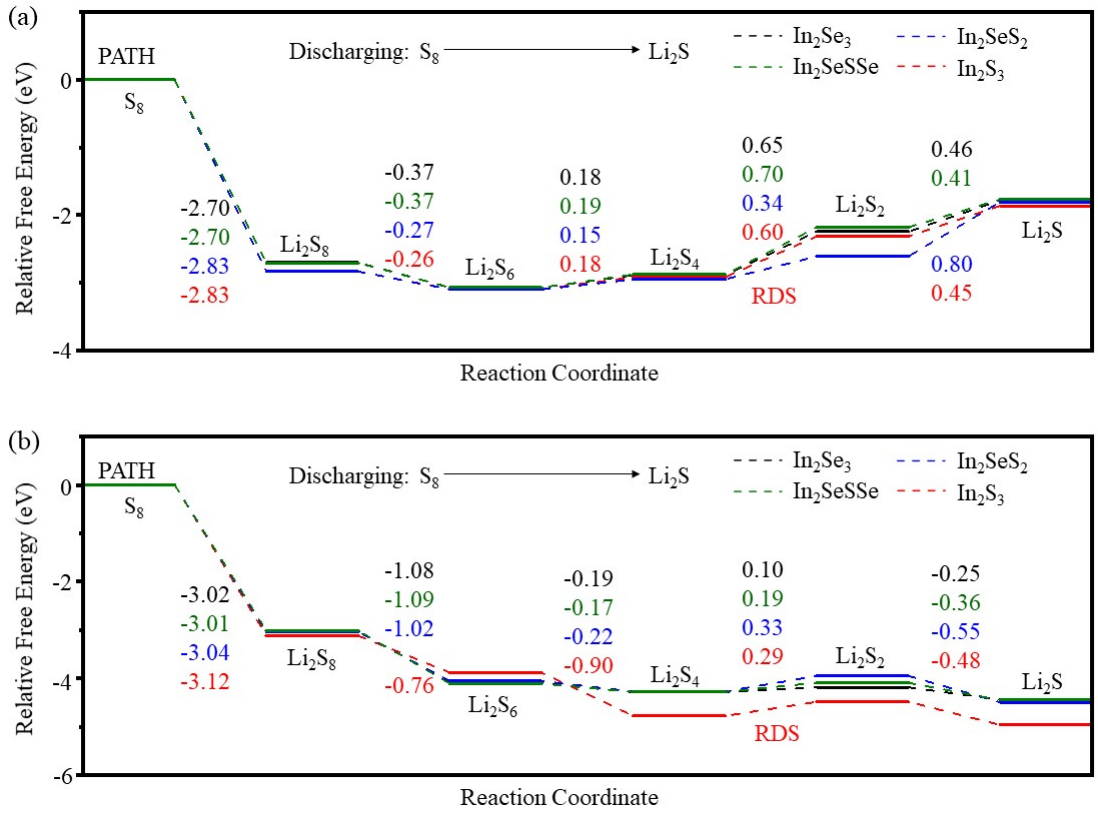

Figure S10. Comprehensive catalytic performance analysis of $In_2Se_nS_{3-n}$ catalysts for lithium-sulfur batteries. (a) Gibbs free energy diagram of the SRR on an $In_2Se_nS_{3-n}$ catalyst after ferroelectric reversal, indicating the rate-determining step (RDS) as Li_2S_4 → Li_2S_2. (b) Gibbs free energy diagram for the SRR on a two-dimensional $In_2Se_nS_{3-n}$ catalyst with surface defects, indicating the rate-determining step (RDS) as Li_2S_4 → Li_2S_2.

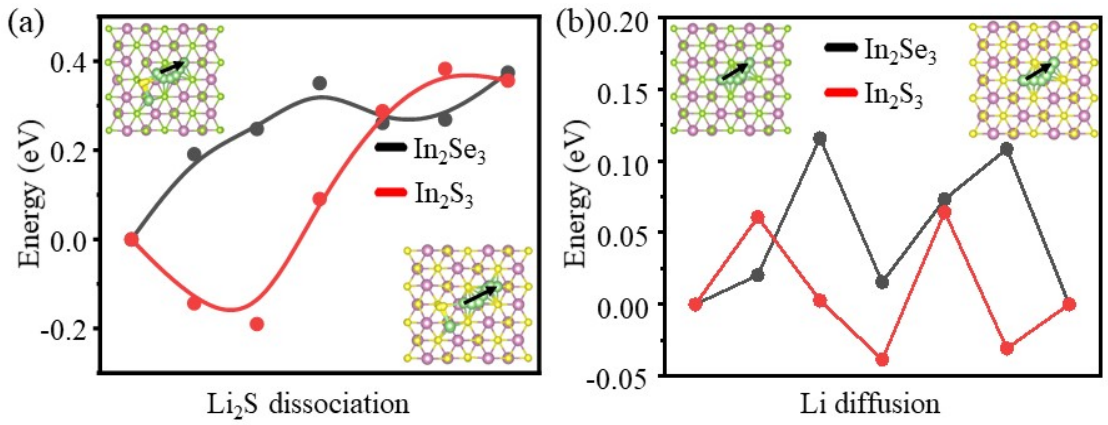

Figure S11. Comparative analysis of Li_2S decomposition kinetics and Li diffusion on In_2Se_3 and In_2S_3 catalyst surfaces. (a) Calculated energy barriers for the decomposition of Li_2S on In_2Se_3 and In_2S_3 surfaces. Corresponding molecular configurations of the compounds are shown on the right. (b) Diffusion pathways and the associated energy barriers for Li on the surfaces of In_2Se_3 and In_2S_3 catalysts.

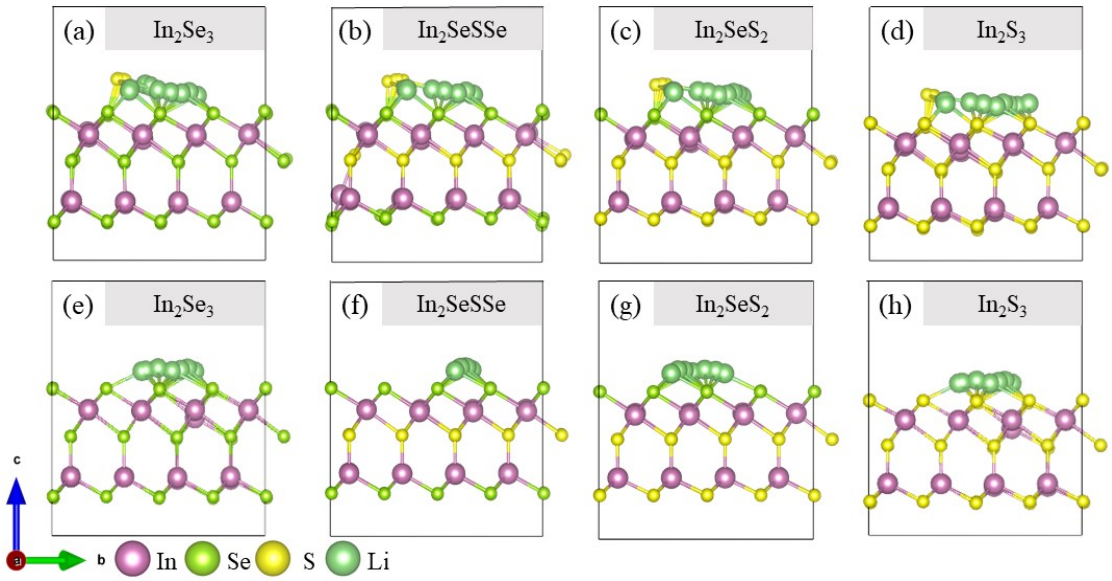

Figure S12. Schematic illustrations of the decomposition and Li diffusion pathways on $In_2Se_nS_{3-n}$ monolayers. Side views of the atomic configurations along the representative decomposition pathways for Li_2S on (a) In_2Se_3, (b) In_2SeSSe, (c) In_2SeS_2, and (d) In_2S_3 surfaces. The reaction coordinate proceeds from left to right in each panel. Side views of the optimized migration pathways for a Li on (e) In_2Se_3, (f) In_2SeSSe, (g) In_2SeS_2, and (h) In_2S_3 surfaces. The diffusion direction is indicated by arrows.

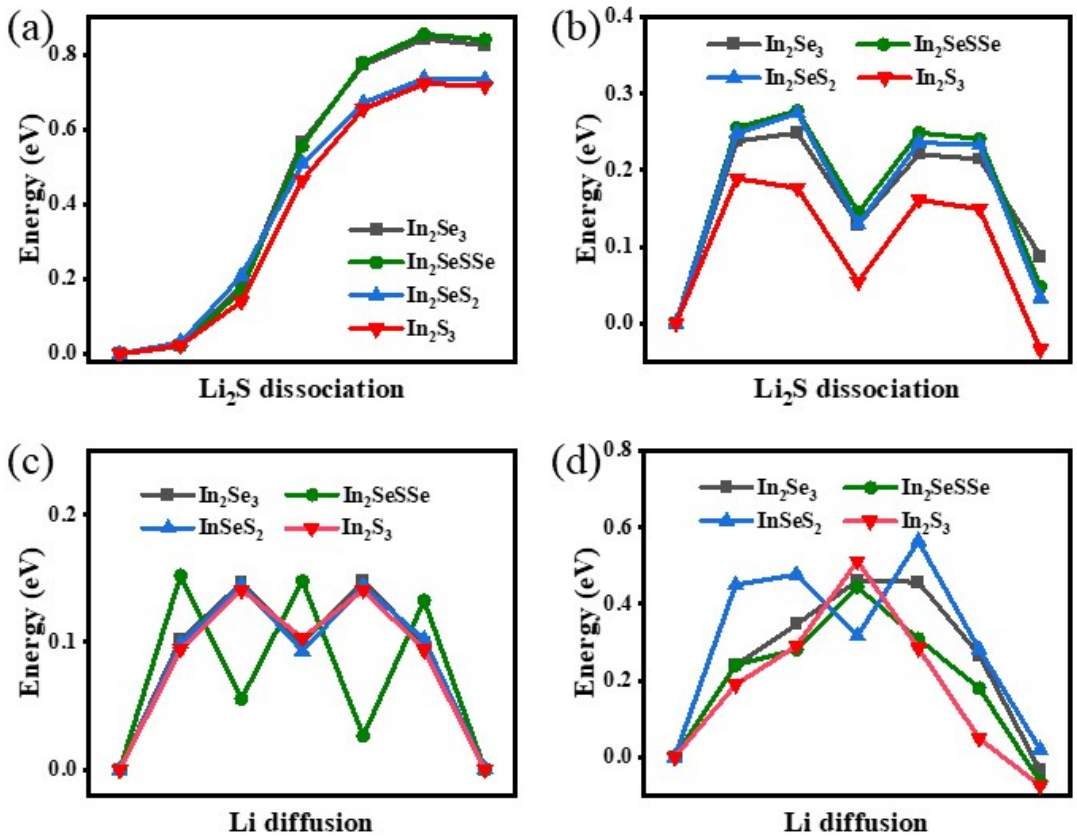

Figure S13. Comparative analysis of Li_2S decomposition kinetics and Li diffusion on $In_2Se_nS_{3-n}$ catalyst surfaces. (a) Surface dissociation energy barrier of Li_2S on $In_2Se_nS_{3-n}$ after ferroelectric reversal. (b) Surface dissociation energy barrier of Li_2S on $In_2Se_nS_{3-n}$ with surface defects. (c) Surface diffusion energy barrier of Li on $In_2Se_nS_{3-n}$ after ferroelectric reversal. (d) Surface diffusion energy barrier of Li on $In_2Se_nS_{3-n}$ with surface defects.

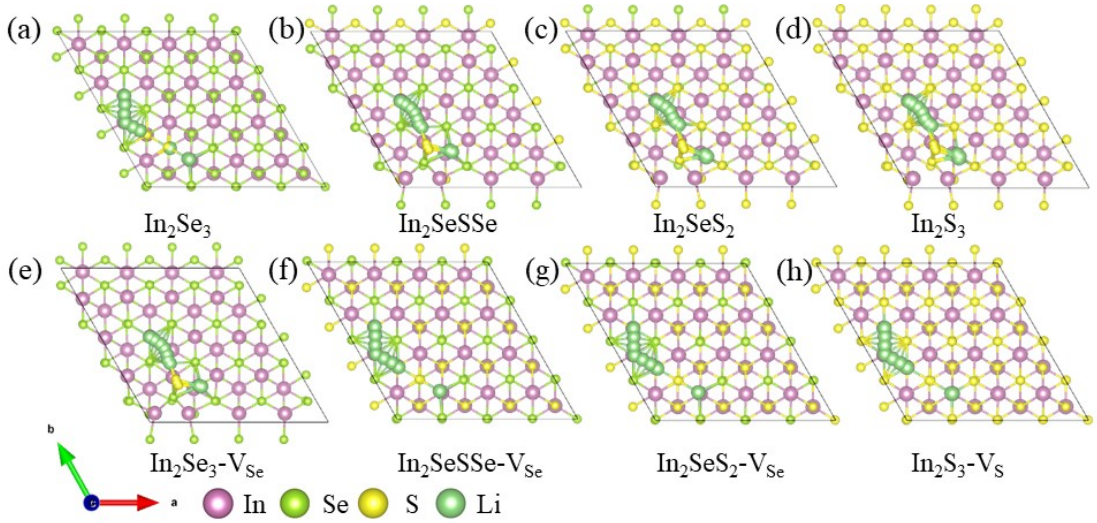

Figure S14. Schematic illustrations of the Li_2S decomposition and Li diffusion pathways on $In_2Se_nS_{3-n}$ monolayers. Atomic configurations along the representative decomposition pathways for Li_2S on (a) In_2Se_3, (b) In_2SeSSe, (c) In_2SeS_2, and (d) In_2S_3 surfaces after ferroelectric reversal. Optimized migration pathways for a Li on (e) In_2Se_3, (f) In_2SeSSe, (g) In_2SeS_2, and (h) In_2S_3 surfaces after ferroelectric reversal.

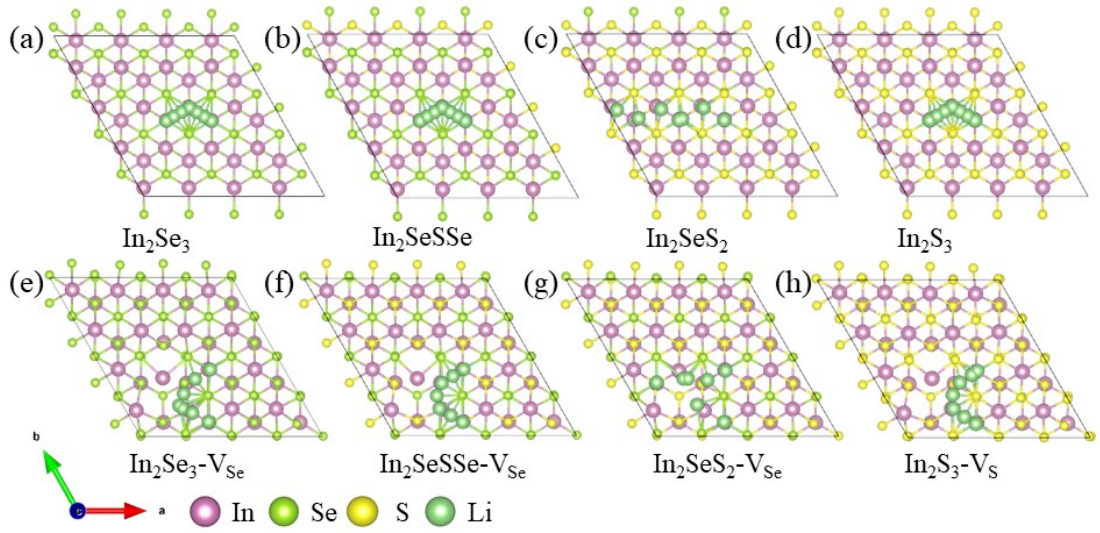

Figure S15. Schematic illustrations of the Li_2S decomposition and Li diffusion pathways on $In_2Se_nS_{3-n}$ monolayers. Atomic configurations along the representative decomposition pathways for Li_2S on (a) In_2Se_3, (b) In_2SeSSe, (c) In_2SeS_2, and (d) In_2S_3 surfaces with surface defects. Optimized migration pathways for a Li on (e) In_2Se_3, (f) In_2SeSSe, (g) In_2SeS_2, and (h) In_2S_3 surfaces with surface defects.

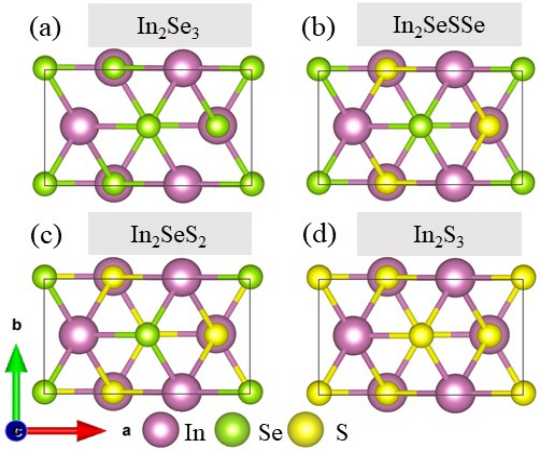

Figure S16. Crystal structure models of two-dimensional $In_2Se_nS_{3-n}$ compounds for electronic transport calculations. Schematic top-view illustrations of the unit cells for (a) In_2Se_3, (b) In_2SeSSe, (c) In_2SeS_2, and (d) In_2S_3 monolayers. The red and blue arrows indicate the crystallographic axes a (horizontal) and b (vertical) in the 2D plane, respectively. These atomic models serve as the input structures for first-principles calculations of electronic transport properties.

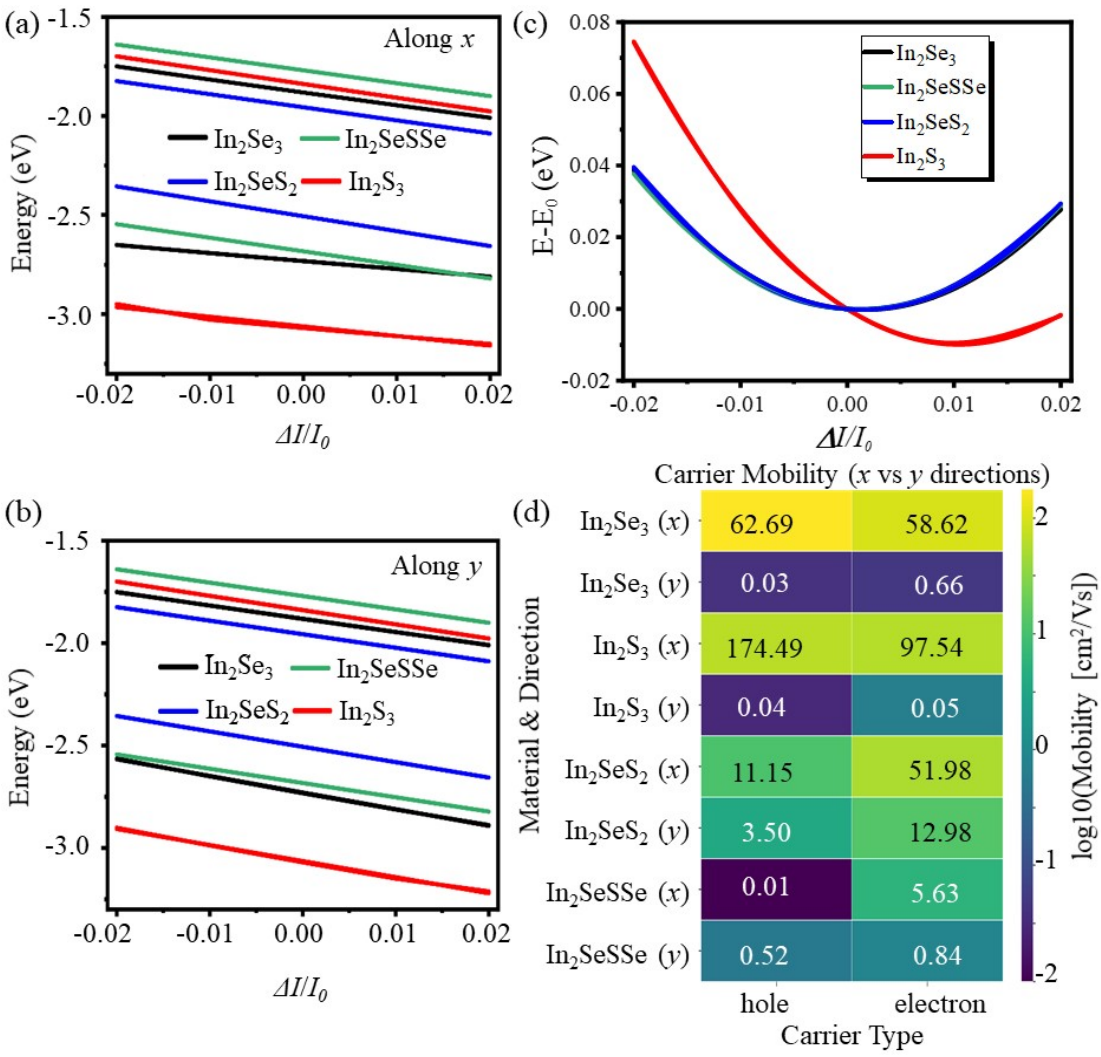

Figure S17. Strain-induced electronic property changes in monolayer $In_2Se_nS_{3-n}$. Energy shift of the (a) VBM and (b) CBM relative to the vacuum level (set to 0 eV) as a function of biaxial strain ($\Delta l/l_0$) along the a- and b-axis directions, respectively. (c) Change in total energy per unit area ($E-E_0$) as a function of biaxial strain ($\Delta l/l_0$). (d) Anisotropic carrier mobility represented as a 2D heat map, comparing the calculated electron and hole mobilities along the crystallographic *x*- and *y*-directions for each material.

REFERENCES

1. G. Kresse and J. Furthmüller, *Phys. Rev. B*, 1996, **54**, 11169-11186.
2. G. Kresse and J. Furthmüller, *Computational Materials Science*, 1996, **6**, 15-50.
3. P. E. Blöchl, *Physical Review B*, 1994, **50**, 17953-17979.
4. G. Kresse and D. Joubert, *Physical Review B*, 1999, **59**, 1758-1775.
5. J. P. Perdew, K. Burke and M. Ernzerhof, *Phys. Rev. Lett.*, 1996, **77**, 3865.
6. S. Grimme, J. Antony, S. Ehrlich and H. Krieg, *The Journal of Chemical Physics*, 2010, **132**, 154104.
7. H. Yuan and Y. W. Zhang, *Acs Applied Materials & Interfaces*, 2022, **14**, 16178-16184.
8. X. Song, Y. Qu, L. Zhao and M. Zhao, *Acs Applied Materials & Interfaces*, 2021, **13**, 11845-11851.